Single-Step Direct Laser Writing of Multimetal Oxygen Evolution Catalysts from Liquid Precursors

Shannon McGee[1#], Yu Lei[2,3,4#], James Goff[5], Collin Wilkinson[5], Nabila Nabi Nova[1], Cody Matthew Kindle[1], Fu Zhang[3,4,5], Kazunori Fujisawa[6], Edgar Dimitrov[2,4], Susan B. Sinnott[1,5,7,8], Ismaila Dabo[5,7,8], Mauricio Terrones[1,2,3,4,5,6], Lauren D. Zarzar[1,5,7*]*

[1]Department of Chemistry, The Pennsylvania State University, University Park, Pennsylvania 16802, United States; [2]Department of Physics, The Pennsylvania State University, University Park, Pennsylvania 16802, United States; [3]Center for Atomically Thin Multifunctional Coatings, The Pennsylvania State University, University Park, Pennsylvania 16802, United States; [4]Center for 2-Dimensional and Layered Materials, The Pennsylvania State University, University Park, Pennsylvania 16802, United States; [5]Department of Materials Science and Engineering, The Pennsylvania State University, University Park, Pennsylvania 16802, United States; [6]Research Initiative for Supra-Materials, Shinshu University, Wakasato 4-17-1, Nagano, 380-8553, Japan; [7]Materials Research Institute, The Pennsylvania State University, University Park, Pennsylvania 16802; [8]Penn State Institutes of Energy and the Environment, The Pennsylvania State University, University Park PA 16802, United States. # The authors S.M. and Y.L. contributed equally in this article. *To whom correspondence should be addressed: ldz4@psu.edu (L.Z.), mut11@psu.edu (M.T.)

ABSTRACT. We investigate a laser direct-write method to synthesize and deposit metastable, mixed transition metal oxides and evaluate their performance as oxygen evolution reaction catalysts. This laser processing method enabled the rapid synthesis of diverse heterogeneous alloy and oxide catalysts directly from cost-effective solution precursors, including catalysts with a high density of nanocrystalline metal alloy inclusions within an amorphous oxide matrix. The nanoscale heterogenous structures of the synthesized catalysts were consistent with reactive force-field Monte Carlo calculations. By evaluating the impact of varying transition metal oxide composition ratios, we created a stable $Fe_{0.63}Co_{0.19}Ni_{0.18}O_x$/C catalyst with a Tafel slope of 38.23 mV dec^{-1} and overpotential of 247 mV, a performance similar to that of IrO_2. Synthesized $Fe_{0.63}Co_{0.19}Ni_{0.18}O_x$/C and $Fe_{0.14}Co_{0.46}Ni_{0.40}O_x$/C catalysts were experimentally compared in terms of catalytic performance and structural characteristics to determine that higher iron content and a less crystalline structure in the secondary matrix decreases the charge transfer resistance and thus is beneficial for electrocatalytic activity. This conclusion is supported by density-functional theory calculations showing distorted active sites in ternary metal catalysts are key for lowering overpotentials for the oxygen evolution reaction.

KEYWORDS: laser writing, multimetal catalysis, oxygen evolution reaction

30

31

Developing alternative energy sources that are clean and renewable is imperative for the future, as non-renewable resources will continually deplete, energy consumption is projected to rise, and harmful environmental impact is of increasing concern.[1] The electrolytic splitting of water to produce hydrogen and oxygen fuel provides a sustainable energy source that has recently garnered significant research and application interest.[2–5] The water splitting mechanism is comprised of two half reactions: the hydrogen evolution reaction (HER) and the oxygen evolution reaction (OER). While the theoretical minimum voltage difference to drive these reactions is 1.23 V,[3] the practical cell voltage is in the range of 1.8 to 2.0 V, largely due to the high overpotential of the OER process.[3,4] An efficient and cost-effective catalyst is thus necessary to lower this overpotential. Historically, the best performing OER catalysts have been those containing noble metals, such as IrO_2 and RuO_2; however, Ir and Ru are relatively rare and expensive, making them impractical for long term, high-volume use.[6] Recently, density-functional theory (DFT) was used to predict that by combining W, Fe, and Co to create ternary transition metal oxyhydroxides, improved adsorption energies for OER intermediates could be achieved.[4] Additional theoretical and experimental studies with various multimetal oxides combining Co, Fe, Ni, or Mn have been similarly promising.[7–11] Hence, non-precious, multimetal OER catalysts are possible material candidates with superior cost-effective performance when compared to traditional single metal catalysts.[3]

The performance of transition metal OER catalysts is dependent on their ability to form OER intermediates (*OH, *O, and *OOH) on their surfaces, with the O to OH adsorption energy difference being the main determinant for the observed activity trends among catalyst materials.[3,4] Relationships between the crystalline structure of the active sites in transition metal catalysts and the OER activity are often established by examining trends in the binding energies of OER reaction intermediates.[10,12–14] The oxidation state of the metals Fe^{3+}, Co^{3+}, and Ni^{2+} are the most predominately studied due to their ability to form optimal M-O adsorption bonds to the catalyst surface to form OER intermediates.[7,8,15] Previous studies have shown that combining these three elements together improves catalytic activity, as Fe is able to stabilize Ni in the 2+ oxidation state which is beneficial for OER activity, while Co is able to lower the charge transfer resistance of the catalyst.[7,8] Transition metal catalysts such as FeNi layered double hydroxides[6,16] and FeCo oxides[17–19] have yielded OER catalytic performances approaching that of precious metal oxide standards of IrO_2 and RuO_2 due to their ability to adsorb hydroxy or oxygen ions by forming M-O bonds to facilitate oxygen production (**Table S1**).[3] Gelled FeCoW oxyhydroxide is currently one of the best OER transition metal catalysts with an overpotential of 223 mV and Tafel slope 37 dec^{-1} (**Table S1**).[4] Achieving a high degree of homogeneity in the mixed transition metal oxides while also maintaining low levels of bulk sample crystallinity has been shown to create lattice distortions that are key to forming beneficial M-O adsorption bonds by augmenting the density of active transition metal sites in the catalyst and modulating the stability of the OER intermediates.[3,20]

Exploration of different processing approaches can facilitate the discovery of phases and structures of multimaterial catalysts and their active sites that might be difficult to access *via* common synthetic routes such as impregnation, electrodeposition, and precipitation methods.[3,4,7,8,15,21] For example, a study done in *Science* by Zhang *et al.* demonstrated how a multimetal catalyst of FeCoW was processed through an annealing synthesis method or through a contrasting sol-gel synthesis method where the sol-gelled FeCoW catalyst had an optimized OER performance.[4] As it is still largely unknown how the specific catalyst structure in more complex mixed metal oxides affects activity, small variations in the catalyst processing method can have dramatic influence over performance, especially for those methods

which form amorphous, nanocrystalline, or metastable phases that are more ill-defined or disordered.[3] We have recently developed a laser writing process to synthesize and pattern a wide range of metal oxide materials from inexpensive precursor solutions with high homogeneity and nano-crystallinity which holds promise for catalyst synthesis.[22,23] In this process, a titanium:sapphire laser is focused through an objective lens into a precursor solution to create a high temperature, microscale solvothermal reactor, termed a laser-induced thermal voxel (LITV), with temperatures likely reaching 600-1000 °C within the femtoliter focal volume.[22,23] Precursor compounds in the solution are thermally decomposed to produce nanoparticle composites which become sintered to the substrate while the laser is scanned.[22,23] Mixtures of fluid precursors can be easily used to create nanocomposites of tunable composition.[23] This processing method may enable the rapid synthesis of multi-component catalysts which are metastable and difficult to fabricate by other means.

Here we demonstrate that the LITV method is a promising synthetic route to facilely create metal oxides and mixed metal oxides that have excellent performance as OER catalysts. Through changing the fluid elemental precursor ratio, we varied the atomic composition of mixed metal oxide catalysts to target optimal OER performances and study how the ratio of Fe, Co, and Ni affects catalytic behavior. The best catalyst for OER was $Fe_{0.63}Co_{0.19}Ni_{0.18}O_x$/C with 38.23 mV dec^{-1} and 247 mV for Tafel slope and overpotential, respectively. Transmission electron microscopy (TEM) and energy dispersive x-ray spectroscopy (EDS) characterization of the catalysts show a complex nanoscale structure composed of a mixed metal ternary alloy within a primarily amorphous iron oxide matrix, a structure whose formation was supported by reactive force-field Monte Carlo simulations. Modification of the degree of crystallinity through annealing studies demonstrate the importance of the amorphous matrix for enhanced catalytic performance. By studying the mechanism of OER in the $Fe_{0.63}Co_{0.19}Ni_{0.18}O_x$/C catalyst *via in-situ* Raman spectroscopy, we elucidated that the catalyst is able to form metastable phases of NiOOH to facilitate oxygen production, leading to improved performance. We perform electronic-structure DFT calculations to understand how the transition metal composition of Fe, Co, and Ni influence the active site on OER intermediate adsorption and overpotentials for the conventional single-site mechanism. Through this work, LITV synthesis was demonstrated to be a powerful method for screening OER catalysts with complex structures and active sites that are beneficial to OER catalyst performance and provide key insight as to catalyst design and structure-activity relationships.

RESULTS AND DISCUSSION

Since materials containing Fe, Ni, and Co have previously exhibited promising activity as OER catalysts, particularly due to their binding affinity to hydroxy groups to facilitate oxygen formation,[6,16,20] we first aimed to explore whether the LITV method could be used to synthesize mixed metal oxides containing these elements in various ratios (**Figure 1a-b**). We used ethylene glycol solutions containing 1 M $Fe(NO_3)_3$, $Co(NO_3)_2$, $Ni(NO_3)_2$, and mixtures of different volume ratios thereof, as precursors. Nitrate salts were chosen due to their high solubility and results from previous research demonstrating their successful use to create iron, cobalt, and nickel oxides using the LITV method.[23] Ethylene glycol was used as the solvent to enhance structure porosity.[22,23] A droplet of the precursor solution was placed onto a fluorine-doped tin oxide (FTO)-coated glass substrate, and a continuous wave 760 nm Ti:S laser (280 mW) was focused with a 40×, 0.60 NA objective lens onto the interface between the glass substrate and precursor solution. Thermal decomposition of the precursors inside the thermal voxel generated continuous deposition of material as the laser was scanned. A description of the optical setup and laser scanning

parameters is provided in the Methods section. To deposit a different material, the substrate was rinsed, and a new precursor solution was placed on top of the substrate. The resultant materials deposited from the single, binary, and ternary combinations of precursors were analyzed with scanning electron microscopy (SEM) and energy dispersive x-ray spectroscopy (EDS) (**Figure 1c-f**). The EDS results confirm that we could deposit the single, binary, and ternary elemental catalysts, which exhibited homogeneous elemental mixing of Fe, Co, and Ni on the sub-micron scale (**Figure 1d-f**). However, the elemental ratios of Fe, Co, and Ni in the deposited materials were not necessarily reflective of the input ratios of the precursors; while the binary and ternary catalysts in **Figure 1** were deposited from equimolar input ratios of the precursors, the output composition of the resultant metals in the deposited materials as determined by EDS analysis were: $Fe_{0.72}Co_{0.28}O_x/C$, $Fe_{0.55}Ni_{0.45}O_x/C$, $Co_{0.64}Ni_{0.46}O_x/C$, and $Fe_{0.63}Co_{0.19}Ni_{0.18}O_x/C$. More in-depth analysis was investigated between the binary elemental combinations by studying the relationship between the feeding input of precursor solutions and the resulting material output for Fe-Ni, Fe-Co, and Co-Ni in **Figure S1'**. The deposits contain carbon as confirmed by Raman spectroscopy which likely originates from the ethylene glycol solvent (**Figure S2**).

To supplement the ratios seen by EDS, we conducted a depth profile study of the $Fe_{0.63}Co_{0.19}Ni_{0.18}O_x/C$ sample using x-ray photoelectron spectroscopy (XPS) to a maximum depth of ~1.2 μm. The depth profile results show that at the surface there is a higher amount of carbon and small amounts of Fe, Co, and Ni. As we etch further into the sample, Fe comes out at a higher concentration than Co and Ni in the order of Fe>Co>Ni for concentration. This is similar to the trends described in **Figure S1**. The atomic ratios determined in the pre-sputter survey spectrum are C 1s (45%), O 1s (44%), Fe 2p (5%), Co 2p (4%), and Ni 2p (2%). The atomic ratios calculated in the post-sputter spectrum are C 1s (11%), O 1s (42%), Fe 2p (27%), Co 2p (14%), and Ni 2p (5%). The elemental ratios of Fe, Co, and Ni in the pre-sputter to post-sputter survey spectra demonstrate the presence of deposited carbon species on the surface and the deposition trend of Fe>Co>Ni in the catalyst. This data supports the evidence seen previously in **Figures S1-S2**. Comparing the EDS ratio of the elements Fe, Co, and Ni in catalyst 1 ($Fe_{0.63}Co_{0.19}Ni_{0.18}O_x/C$) with the determined XPS ratio ($Fe_{0.59}Co_{0.30}Ni_{0.11}O_x/C$) shows similar ratio trend with considerably more Fe than Co and Ni, and Co being in higher amount than Ni. Differences in these exact ratio values (particularly in reference to the amount of Co) suggest that there is more Co nearer to the surface when taking into account the depth of signal penetration for XPS (30 nm) compared to EDS (2 μm). However, both EDS and XPS have associated error in the measurement (±5% and ±10% respectively), and we will show later that the samples themselves have a heterogeneous structure which could cause fluctuations in the elemental measurement.

120 Having confirmed that we could direct-write Fe-, Co-, and Ni-containing materials by LITV, we next aimed to test their

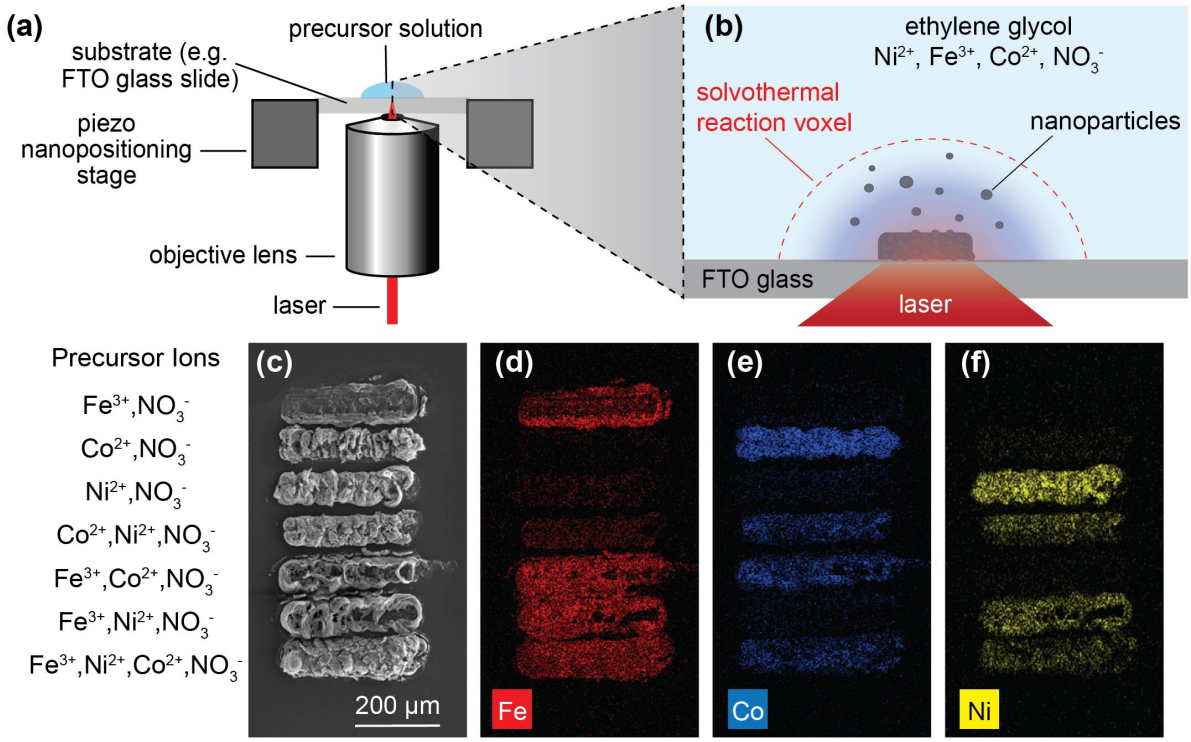

Figure 1. The LITV method was used to synthesize and direct-write mixed metal oxides from fluid precursors. (a) Schematic of the LITV process; a continuous wave Ti:S laser (760 nm) is focused through an objective lens onto the surface of a substrate (*e.g.* FTO glass) covered with fluid precursor. Absorption of the laser produces a steep, localized thermal gradient, *i.e.* "reaction voxel" **(b)** where the precursors are thermally decomposed and deposited onto the substrate in a solid film as the laser is scanned. **(c)** SEMs of single, binary, and ternary metal oxides and mixed metal oxides of Fe, Co, and Ni as prepared from solutions containing the ions listed at left. Scale bar, 200 µm. **(d-f)** SEM-EDS maps showing the distribution of Fe, Co, and Ni elements corresponding to the same sample shown in **(c)**.

121 performance as OER catalysts and compare the performance as a function of composition. LITV was used to deposit 1 × 1 mm squares of
122 the single, binary, and ternary elemental catalysts onto FTO-coated glass, where all precursors were in ethylene glycol and contained 1 M
123 total nitrate salts with varying elemental ratios of Fe, Ni, and Co. To determine each material's OER catalytic efficiency, we tested each
124 catalyst for three cycles with linear sweep voltammetry (LSV) in 1 M KOH to measure Tafel slope and overpotential at 10 mA cm^{-2} (**Figure**
125 **2a-b**). A table showing the datapoints from **Figure 2a-b**, including the precursor ratios, the materials' elemental composition determined

by EDS, and OER overpotential and Tafel slope, are given in **Table S2**. In general, we found that the single-component catalysts tended to have poor performance, with high Tafel slopes and overpotentials for OER. Varying the ratios of Ni and Co in binary $Ni_xCo_yO_z$/C catalysts did not seem to enable significant reduction of the overpotential, but the introduction of Fe into ternary catalysts yielded a notable improvement in performance; the best OER performance (38.23 mV dec^{-1} and 247 mV for Tafel slope and overpotential respectively) was found in the $Fe_{0.63}Co_{0.19}Ni_{0.18}O_x$/C catalyst (**catalyst 1**), which was produced with equimolar ratios of the respective 1 M metal nitrates in ethylene glycol. To test **catalyst 1**'s stability, we used cyclic voltammetry to analyze **catalyst 1**'s polarization curve for 5000 cycles and witnessed no decay in performance (**Figure S3a**). This OER performance is comparable to other high-performing catalysts reported in the literature, including gelled FeCoW and IrO_2 (overpotential 223 and 260 mV and Tafel slope 37 and 45 mV dec^{-1} respectively).[4,6,15]

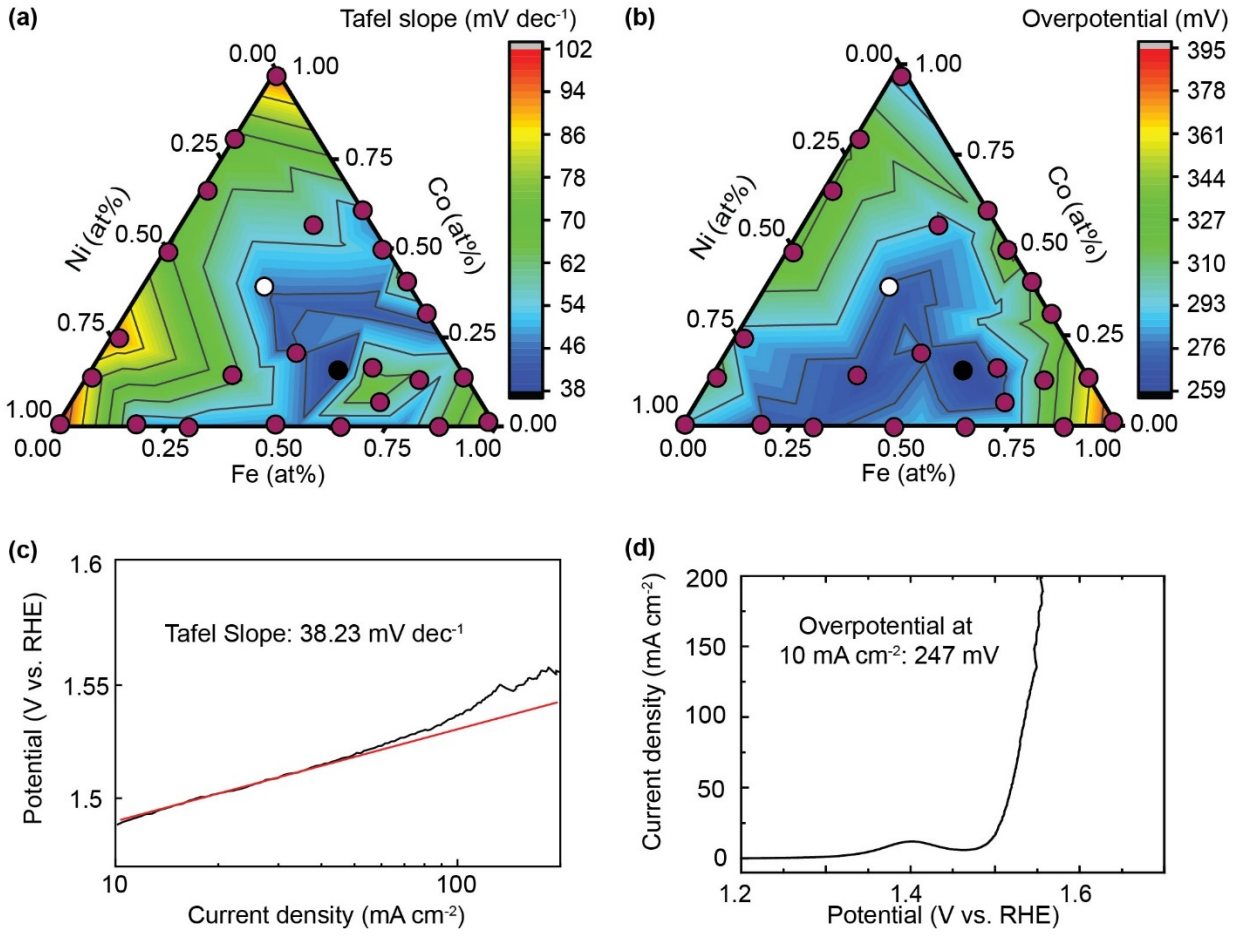

Figure 2. OER performance determined by LSV for Fe, Co, Ni multimetal catalysts fabricated by LITV. Correlation of Ni, Fe and Co atomic percentage in the catalyst as determined by EDS with **(a)** the Tafel slope and **(b)** the overpotential measured at 10 mA cm^{-2}. The contour plots **(a, b)** of kinetic parameters, Tafel slope and overpotential at 10 mA cm^{-2}, were extracted from the Tafel and polarization plots on 26 independent catalysts. Circles indicate experimental datapoints, with the black circle indicating our best performing catalyst material, **catalyst 1** ($Fe_{0.63}Co_{0.19}$ $Ni_{0.18}O_x$/C), and the white circle indicating a ternary catalyst with comparatively less Fe content, **catalyst 2** ($Fe_{0.14}Co_{0.46}Ni_{0.40}O_x$/C), which has less catalytic efficiency. **Table S2** includes all the datapoints from **(a,b)**. **(c)** Tafel slope fitted with linear

regression (red line) and **(d)** OER polarization curve verses the reversible hydrogen electrode (RHE) of **catalyst 1** in 1 M KOH. The Tafel slope is 38.23 mV dec^{-1} and the overpotential is 247 mV.

In order to probe the origins of the improved OER performance in binary and ternary catalysts, electric impedance spectroscopy (EIS) and electrochemical surface area (ECSA) were carried out as seen in **Figure S3b-c**. As indicated by EIS shown in **Figure S3b**, the decrease in the Nyquist plot semicircle radius for binary and ternary catalysts with Fe ($Fe_{0.78}Ni_{0.22}O_x$/C, $Fe_{0.81}Co_{0.19}O_x$/C, and **catalyst 1**), compared to the catalyst without Fe ($Co_{0.64}Ni_{0.36}O_x$/C), suggests that the Fe is able to significantly lower the charge transfer resistance of the material. As seen in **Figure S3c**, the addition of Fe and Co together in a binary and ternary catalyst ($Fe_{0.81}Co_{0.19}O_x$/C and **catalyst 1** respectively) is able to increase the ECSA by 4-fold compared to the ECSA of $Co_{0.64}Ni_{0.36}O_x$/C, indicating more electrochemically accessible area in these materials. Thus, the addition of Fe in the alloy is able to lower the charge transfer resistance and the presence of Fe and Co together exposes more accessible active sites in $Fe_wNi_xCo_yO_z$/C ternary catalysts. These results support the observation that the overpotential and Tafel slope are largely influenced by the ratio of Fe in relation to Co and Ni, and is relevant for catalytic activity (**Figure 2**).

To experimentally determine the differences in performance in relation to structural and elemental composition of the synthesized ternary catalysts, we used TOF calculations, X-ray photoelectron spectroscopy (XPS), X-ray diffraction (XRD), scanning transmission electron microscopy (STEM), and high-resolution scanning transmission electron microscopy (HRTEM) to compare the best performing catalyst (**catalyst 1**) with **catalyst 2** ($Fe_{0.14}Co_{0.46}Ni_{0.40}O_x$/C). **Catalyst 2** was chosen for purposes of comparison because, similar to **catalyst 1**, it also contained Ni and Co in an atomic ratio where Co>Ni, but it had proportionally less Fe than both Co and Ni. The OER performance of **catalyst 2** was notably worse than **catalyst 1**, with an overpotential of 284 mV and Tafel slope of 54.46 mV dec^{-1} (**Table S2**). The intrinsic OER electrocatalytic activity of these two catalysts is also reflected by the turnover frequency (TOF). By assuming that all the metal cations are the reactive sites, the TOF calculated for **catalyst 1** was 0.0258 O_2 s^{-1} at the overpotential of 350 mV, significantly higher than that of the TOF of **catalyst 2** which is 0.0017 O_2 s^{-1} (calculation detail can be found in the Methods). To continue studying the differences between **catalyst 1** and **2**, we looked into the structural characterization of these materials.

XPS analysis was first used to probe the chemical states of the elements on the surface for **Catalyst 1** and **2** before and after OER testing (**Figures S5-S6** and **S7-S8** respectively). Overall, the analysis shows a combination of metal oxides and hydroxides, as well as strong evidence for metal alloy species. The high resolution oxygen peaks for both catalysts can be fitted with lattice oxygen and surface hydroxyl/ non-stoichiometric oxygen peaks (~530 eV and ~532 eV respectively). These peaks can be attributed to the mixing of the metal oxides creating a non-stoichiometric environment and potential hydroxyl intermediates that formed during the OER reaction.[24–28] XPS shows carbon on the surface originating from the ethylene glycol solvent similar to the previous data seen in the XPS depth profile study and Raman data in **Figure S2-S3**. For both catalysts before and after OER testing, the Fe 2p, Co 2p, and Ni 2p core spectra are split into $2p_{1/2}$ and $2p_{3/2}$ orbital peaks due to spin-orbital coupling.[29–31] The Fe and Co 2p core spectra for both catalysts can be fitted with 3+, 2+, and 0 valence states, providing compelling evidence for the presence of Co_3O_4, Fe_3O_4, and metal alloy species on the surface.[24–28,32] For both

catalysts, the Ni 2p core spectra demonstrate fitted Ni^{2+} and Ni^{0} states as Ni metal and NiO species.[24–28,32] The Fe^{3+}, Co^{3+}, and Ni^{2+} valence states have been shown to have the ability to form optimal M-O adsorption bonds to the catalyst surface to form OER intermediates which could be facilitating the lower overpotentials seen in these ternary catalysts compared to the binary catalysts.[7,8,15] The presence of NiO, Fe_3O_4, and metal Fe, Co, and Ni alloy species seen in the XPS data are also supported by XRD spectra in **Catalyst 1**'s post-OER testing and annealing spectrum (**Figure S10-S11**).

To better compare the differences in these two catalysts, we found in XRD spectra that **catalyst 2** shows higher intensity peaks overall than the peaks in **catalyst 1**'s XRD spectra (**Figure S9a and S10a**), and therefore suggests a more overall crystalline structure in **catalyst 2**. We also found that the XRD diffraction peaks for **catalyst 1** indicate a similar match to a ternary metal alloy reference of $Fe_{0.5}Co_{0.4}Ni_{0.1}$,[33] while **catalyst 2** indicates a similar match to a ternary metal alloy reference of $Fe_{0.33}Co_{0.48}Ni_{0.19}$.[34] While neither catalyst showed metal oxide peaksbefore electrochemical testing, **catalyst 1** exhibited low intensity NiO peaks[35] after electrochemical testing. The presence of NiO explains the peak at ~1.4 V observed in **Figure 2d**, which corresponds to the oxidation reaction of Ni(II)/Ni(III).[16,36] HRTEM measurements of the lattice spacing of the nanocrystalline particles (**Figure S9b, S10b**) yielded spacings of 0.20 nm for **catalyst 1** and 0.18 nm for **catalyst 2**, which match well to their XRD (111) and (200) plane reference values respectively.[33,34] We analyzed both catalysts with STEM and EDS mapping after LSV and observed the presence of particles containing Fe, Ni, and Co (with higher amounts of Ni and Co compared to Fe), dispersed within a primarily iron oxide matrix (**Figure 3a** and **Figure S9b, S10b**). **Catalyst 1** had particle sizes averaging ~10 nm in diameter (**Figure 3a** and **Figure S11**), while **catalyst 2** had a more polydisperse particle size range of ~2-11 nm (**Figure S9b** and **Figure S11**). Although the STEM-EDS and XPS data of both samples show oxygen in the structure, the lack of intensity for any oxide peaks in both catalysts' XRD spectra suggest these oxide structures are amorphous and lack long-range order. In conclusion, there were two main structural differences between **catalyst 1** and the comparative **catalyst 2**: 1) **catalyst 1** has a higher Fe composition than **catalyst 2,** and 2) **catalyst 2** is more crystalline overall. We have experimentally demonstrated that having low Fe content (**Figure 2a-b** and **S4b-c**) can worsen catalytic performance by lowering the ECSA, while increasing the overpotential, Tafel slope, and charge transfer resistance which can reasonably explain why **catalyst 2** has a relatively worse OER performance compared to **catalyst 1**.

To experimentally probe the importance of the amorphous matrix structure, we annealed **catalyst 1** at temperatures between 100 °C and 400 °C under argon for an hour in an attempt to increase the crystallinity of the matrix and examine the effect on the catalytic performance (**Figure S12)**. XRD spectra (**Figure S12a)** indicate that indeed there was an increase of intensity in the crystalline metallic ternary alloy peaks[33] and also the appearance of metallic iron peaks as a result of thermal annealing.[37] We then conducted LSV on **catalyst 1** annealed at different temperatures to determine the corresponding OER performance (**Figure S12b**). Samples annealed at higher temperatures correlated to an increase in the Tafel slope and overpotential and, therefore, a decrease in catalyst efficiency. The charge transfer resistance was also observed by EIS to increase with higher annealing temperature (**Figure S12c)**. Thermal annealing of **catalyst 1** at 400 °C in air, rather than argon, converted the amorphous metal oxide matrix to crystalline magnetite[38] **(Figure S12d)** and similarly yielded worse performance; the Tafel slope and overpotential measured at 10 mV cm^{-2} was 51.07 mV dec^{-1} and 347 mV respectively, which was similar to the performance of the **catalyst 1** sample annealed at 400 °C in argon (**Figure S12b**).

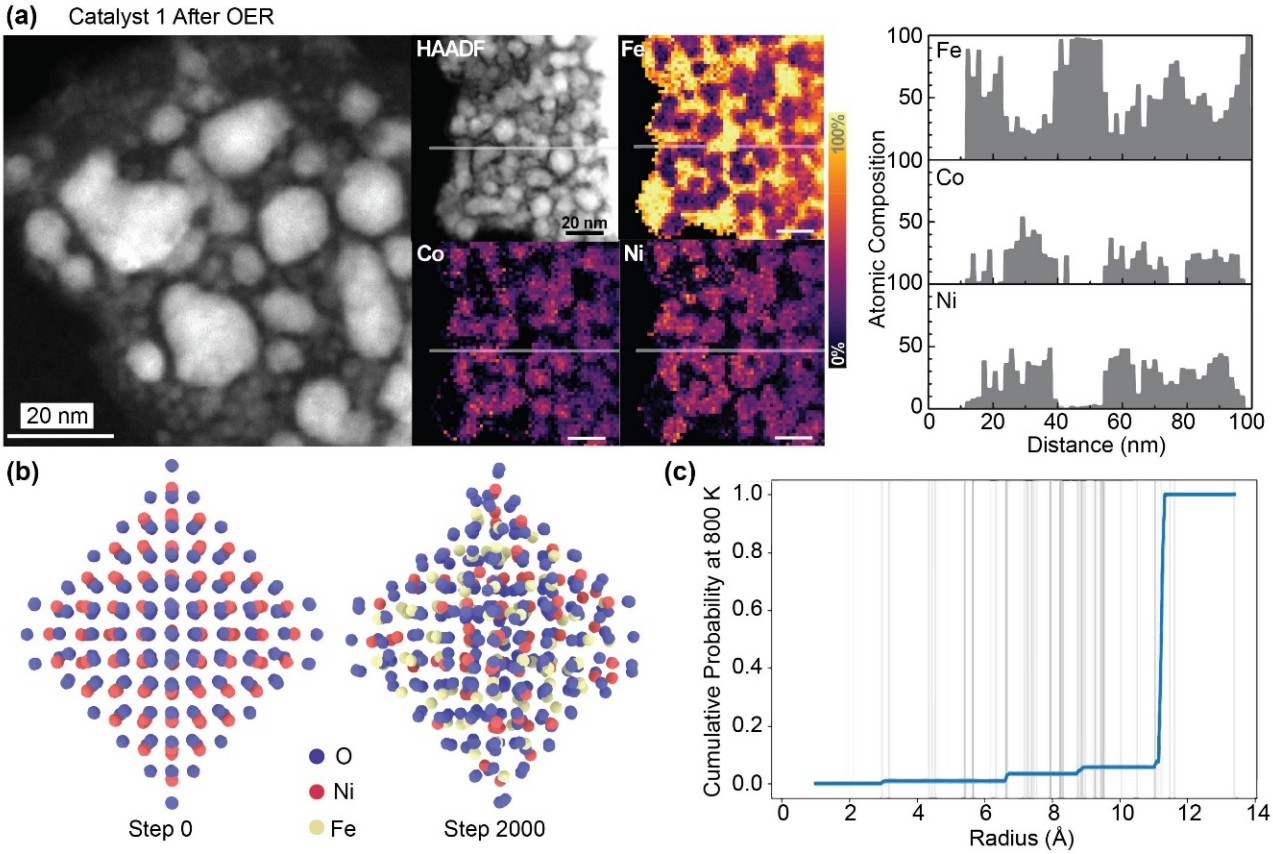

Figure 3. TEM structural characterization of catalyst 1 and Monte Carlo simulation. (a) STEM shows the structure of **catalyst 1** ($Fe_{0.63}Co_{0.19}Ni_{0.18}O_x$/C) after electrochemical testing with LSV. Scale bars, 20 nm. EDS metal distribution of Fe, Co, and Ni suggests localized Fe, Co, and Ni particles within a primarily amorphous iron oxide matrix. Scale bars 20 nm. **(b)** The STEM results are supported by the formation of the secondary amorphous Fe phase in a Monte Carlo simulation carried out across 2000 parameterization steps based on a ReaxFF model for Ni (red), Fe (yellow), and O (blue). Step 0 shows the cubic nickel oxide structure without any ion switching while Step 2000 shows the 2000th iteration of the simulated parameterization steps. This simulation suggests that increasing the Fe content will also increase amorphous character in the structure **(c)** Monte Carlo simulation of the cumulative probability of Fe occupation in a nanoparticle as a function of the radius from the center and temperature at 800 K, with the black lines showing the density of atoms at each radius from the center of the nanoparticle. The Boltzmann weighting shows the high probability of Fe being found at the surface of the particle.

Based on our characterization of **catalyst 1**, the structural composition consisting of nanocrystalline alloy particles embedded with a primarily amorphous iron oxide matrix appeared relevant to the catalytic properties. To understand better how the LITV synthetic method was able to access the formation of this heterogeneous structure, a Monte Carlo simulation was carried out based on a reactive force-field (ReaxFF) model for Ni, Fe, and O, according to **Equations 1** and **2** (see Methods section). The temperature in which the Monte Carlo simulation was carried out was taken to be 1000 K to mimic the high temperatures found at the laser focal point in the thermal voxel and the parameterization step was repeated for 2000 iterations (**Figure 3b**). Due to limitations in current reactive potential available to

incorporate Co with the other three elements, this Monte Carlo analysis neglects Co. By exploring the effects of substituting Fe into a cubic NiO crystalline structure, we observe that over multiple Fe substitutions, the structure becomes more amorphous. The fact that it is more energetically favorable at high temperatures to form an amorphous structure with the addition of Fe into a cubic NiO helps explain the formation of an amorphous phase in our catalysts which are rapidly synthesized at high temperature. The Boltzmann sampling (**Figure 3c** and **Figure S13**) shows that Fe migrates to the surface layers of the nanoparticle to form an amorphous phase due to it being drastically energetically favorable for Fe to form at the interface rather than in the core of the nanoparticle at elevated LITV temperatures. Our calculations suggest that the LITV synthesis method thus yields a complex structure due to the temperature created by the voxel, where the nanoparticle loses its symmetry by creating a kinetically favored amorphous layer with high Fe content outside of the more crystalline particle.

To further compare the electrochemical properties of **catalysts 1** and **2**, we analyzed these two samples using *in-situ* Raman spectroscopy during LSV for determining what intermediates form during OER.[4,15] We found that without electrochemical bias and OER cycling, only weak and broad peaks are found between 300 to 1200 cm^{-1} (**Figure S2**), indicating the presence of highly disordered (and even amorphous) oxides in **catalysts 1** and **2**. This is consistent with the previous structural characterization, which indicated a lack of long-range order and an amorphous matrix surrounding small nanocrystalline metallic particles (which would not be detectible with Raman spectroscopy). Peaks at ~1350 cm^{-1} and ~1600 cm^{-1} in **catalyst 2** correspond to the D- and G-band of carbon-based materials (**Figure S2**). This indicates that more carbon (likely from the ethylene glycol solvent), was deposited in **catalyst 2** when compared to **catalyst 1**, which could result from the higher content of Co and Ni that exhibit greater catalytic reactivity to deposit carbon as compared to Fe.[39] As the potential was increased for **catalyst 1** from 1.07 V to 1.47 V (*vs.* RHE), broad bands at ~ 550 cm^{-1} and ~455 cm^{-1} emerge, indicating the generation of the OER intermediate NiOOH (**Figure 4a**).[12] The intensity ratio of the two bands (I_{455}/I_{550}) also increases to a degree that is commensurate with the applied voltage, indicating the phase transformation from β-NiOOH to γ-NiOOH.[40–42] In comparison, the formation of the OER intermediate NiOOH was not observed for **catalyst 2** (**Figure 4b**), and only an etalon interference signal was witnessed. Given that this NiOOH metastable intermediate can help facilitate oxygen formation in OER[4,15], these results can help explain why **catalyst 2** has poorer OER performance than **catalyst 1**.

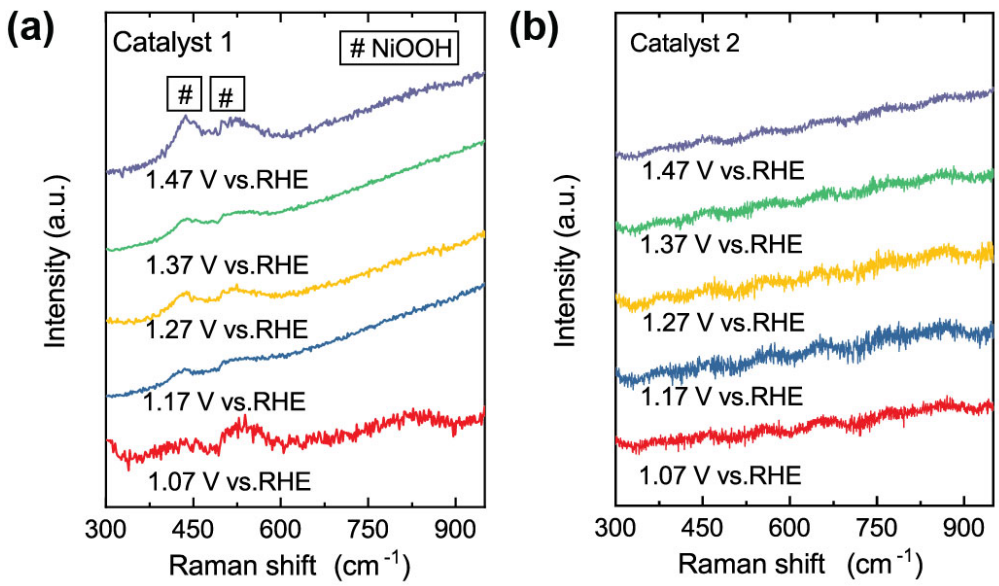

Figure 4. ***In Situ*** **Raman analysis for determination of catalytic intermediates.** *In Situ* Raman spectra using a 532 nm laser line of **(a)** $Fe_{0.63}Co_{0.19}Ni_{0.18}O_x$/C (**catalyst 1**) and **(b)** $Fe_{0.14}Co_{0.46}Ni_{0.40}O_x$/C (**catalyst 2**) with applied electrochemical bias from 1.07 V to 1.47 V *vs.* RHE (reversible hydrogen electrode). The # symbol marks the peak formation indicative of a NiOOH intermediate. For **catalyst 2**, only etalon interference signal was observed.

We conclude from the thermal annealing studies that the complex amorphous matrix of the catalyst plays an important role in enhancing catalytic activity; furthermore, the local transition metal chemistry and heterogeneous crystal structure at the nanoparticle-amorphous matrix interface itself may play a significant role. The influence of the local chemistry and structure of the active sites on the overpotential can be examined using first-principles models. To assess the activity of the varied crystal structures expected at the catalyst interfaces, we predicted the overpotential of the single-site OER mechanism in representative oxides, oxyhydroxides, and doped oxyhydroxides (NiO, β-CoOOH, hexagonal-CoOOH, and hexagonal-CoOOH doped with Ni and Fe added within the first 4 neighbor shells of the active site (**Figure 5a** and **Figure S8**) as based on our previous in situ Raman results (**Figure 4**). The overpotentials were estimated from the largest thermodynamic barrier associated with the reaction intermediates as calculated at the level of meta-GGA+U. Further details about these calculations can be found in the Methods section. The results are compiled in the volcano plot in **Figure 5b** and show the predicted overpotentials as a function of O* and HO* reaction intermediates adsorption energies. While the computational results indicate that Co sites in ternary Fe-Co-Ni oxyhydroxides can yield overpotentials as low as 236 mV through optimal intermediate energetics that are similar to our experimental results in **Figure 2**, the models also show that the binding energy of the reaction intermediates are highly sensitive to the transition-metal configuration one to three neighbor shells away from the active site as well as the crystal structure (**Table S3**). The dependence of the overpotential on the transition metal configuration and crystal structure can be described in terms of the octahedral distortion of the OER site (**Figure 5c**). The octahedral distortion is coupled to the transition-metal composition near the active site.

By calculating the ellipsoidal distortion parameter, which is the variance in the radii of the minimum bounding ellipsoid for the active site polyhedron,[43] we show that the overpotential is correlated with catalytic site distortion. Lower overpotentials, though sensitive to chemistry and crystal structure, generally correspond to structures with more distorted active Co sites and small amounts of Fe in the second neighbor shell (underneath) these sites. This is likely due to crystal field splitting induced by the octahedral distortion; connections between the intermediate energetics and the orbital energies are made in the Supporting Information (**Figure S15-S16**). The ranges of overpotentials for Ni and Fe sites are expected to be higher due to stronger HO-metal bonds.

This trend can be interpreted, at the electronic level, by examining the hybridization of the *d* orbitals of the surface with the *p* states of the oxygen adsorbate (**Figure S14** and **Figure S15**). Octahedral distortion reflects the crystal field splitting induced in different chemical or structural environments and can thus serve as a simple and sensitive measure of the site-specific oxygen affinity. Our observations suggest that, beyond the ability to tune OER activity by adjusting the composition of a given ternary metal mixture, OER performance may be systematically optimized using synthetic routes that deliberately target the formation of distorted catalytic sites and structural defects, such as our LITV technique.

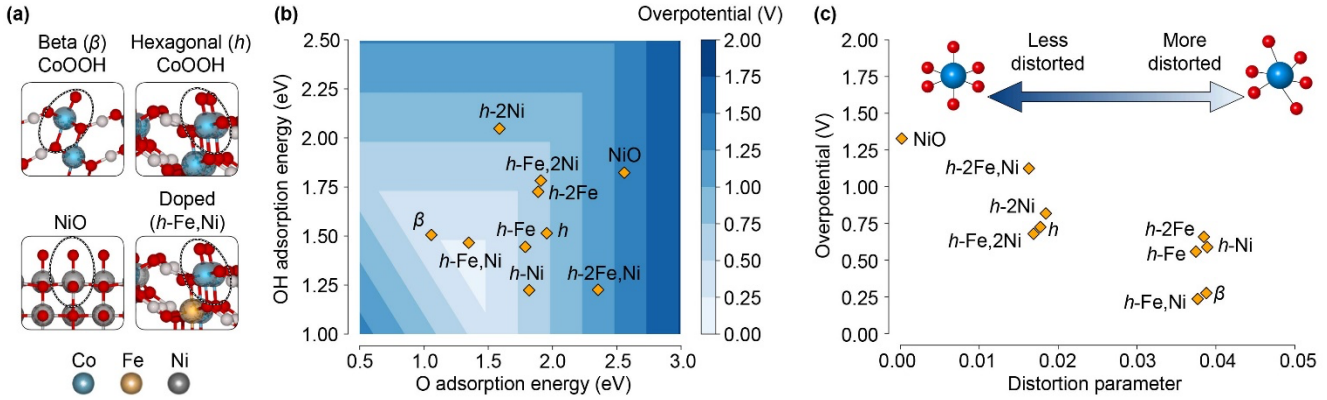

Figure 5. Structural and compositional overpotential trends predicted by DFT. (a) As a proxy for the varied chemical and structural environments in the experimentally produced catalysts, a set of relevant transition metal oxides and hydroxides are sampled to predict single-site OER activity with DFT. The catalytic surface sites are circled for these structures. **(b)** The volcano plot shows the large spread of overpotentials that occur for varied local compositions, crystal structures, and transition metal configurations at oxide surfaces as a function of HO* and O* OER intermediates energetics. The contours in this plot are produced with linear scaling relationships between compositions. The large spread of overpotentials can be simplified by analyzing the structure **(c)**. The ellipsoidal distortion parameter of the active OER site octahedron shows that the overpotential is correlated with the active site distortion; distorted Co and Ni catalyst sites yield lower overpotentials.

CONCLUSIONS

In conclusion, we have discovered that the LITV method can be used to rapidly synthesize metastable mixed metal oxide materials that exhibit promising performance as OER catalysts and propose that enhanced catalytic activity originates from distorted active sites at

the interface of crystalline nanoparticles and an amorphous matrix. The facile nature of LITV processing, including the use of liquid chemical precursors, enabled us to produce a diverse array of catalytic materials containing Fe, Ni, and Co in varying ratios in a cost-effective and timely manner. The complex structure of the ternary catalysts produced from LITV synthesis contained nanocrystalline particles surrounded by a secondary amorphous matrix which we conclude helps to create distorted active sites and is key to lower overpotentials and improved OER performance. Electronic-structure calculations revealed that distorted ternary active sites of Fe, Ni, and Co may reduce the overpotentials compared to more crystalline, single-metal active sites. Monte Carlo simulations explained the formation of a secondary amorphous matrix primarily made of iron oxide. Increased crystallinity of the amorphous matrix achieved by annealing led to phase separation of the elemental Fe or the crystallization of iron oxide, thus altering catalytic efficiency. We also found that our catalysts are able to stabilize metal oxyhydroxide metaphases in solution, thereby facilitating the formation of OER intermediate NiOOH and product O_2. Given that processing variations can have significant impacts on catalyst performance, LITV deposition may prove not only to be a facile synthesis method for nanostructured metastable catalysts but may also serve as a tool to finely tune the atomic and structural properties of catalysts rapidly, enabling more systematic understanding of catalytic mechanisms and optimized performance.

METHODS

Materials

All chemicals are commercially available and used as received. $Fe(NO_3)_3 \cdot 9H_2O$ 98.0% (Alfa Aesar), $Ni(NO_3)_2 \cdot 6H_2O$ 98% (Alfa Aesar), $Co(NO_3)_2 \cdot 6H_2O$ (Fisher Scientific), $C_{16}H_{18}ClN_3S \cdot xH_2O$ (methylene blue, BeanTown Chemical), KOH pellets (EMD). All metal and metal oxide precursor solutions were prepared by dissolving the precursor salts in ethylene glycol (99.8%, Alfa Aesar) at 1 M concentrations. Binary and ternary ratio precursor solutions were made by mixing different volumes of the 1 M solutions. Samples were deposited on fluorine doped tin oxide glass substrate (TEC 7) 1" x 1" x 2.2 mm, R: 6-8 ohm/sq (MTI Corp). Electrodes used for linear and cyclic voltammetry were a platinum RDE auxiliary electrode (BASI) as the counter electrode and an Ag/AgCl reference electrode (BASI). Electrochemical testing was carried out in a 5-15 mL cell vial (BASI) with a Teflon cell top (BASI). A gold RDE auxiliary electrode (BASI) was used as the counter electrode during *in Situ* Raman spectroscopy.

Direct laser writing optical setup

All depositions employed a Coherent Mira Optima 900-F titanium:sapphire laser operating at 760 nm in continuous wave mode. The laser output was controlled using a half wave-plate/polarizing beam-splitter pair, with the half wave-plate controlled by a motorized rotation mount (Thorlabs K10CR1) which allowed for tuning of the laser power. The laser focus was translated using a galvo scanner (Nutfield open frame head XLR8 –10 mm clear aperture), which allowed oscillation of the laser spot as it entered a microscope objective (air 40x Nikon Plan Fluor objective with 0.60 NA) situated on an inverted microscope (ASI automated RAMM/ modular infinity microscope system with motorized stage). Lenses were used to collimate and expand the beam to fill the back of the microscope objective. Laser powers reported were measured at the back of the objective.

Material deposition

To initiate laser deposition, there must be an optical absorber present to absorb the laser radiation and induce photothermal heating.[22,23] To create the initial optical absorber, methylene blue was added to the precursor solution containing ethylene glycol and 1 M metal nitrate such that the methylene blue strongly absorbed the incident laser radiation and a small spot (0.0012 mm^2) of metal oxide could be deposited. Once this small absorbing pad of metal oxide was deposited, the solution was removed, substrate rinsed, and a new precursor without the methylene blue was introduced. The laser was again focused through a microscope objective onto the absorbing pad to create the laser induced thermal voxel, thereby depositing material directly from the precursor fluid. Patterns were "drawn" with the laser by both scanning the laser with the galvo mirrors and translating the microscope stage. Laser power of 280 mW as measured at the back of the objective was used. Catalysts were patterned by translating the microscope stage at 5 μm/s in the x and y directions in a snaking pattern with a laser scan rate of 500 μm/s and amplitude of 60 μm back and forth in the y direction using the galvo mirrors. A 1 x 1 mm square area was deposited for linear sweep voltammetry (LSV) testing.

Characterization

X-ray diffraction (XRD): XRD was performed using a PANalytical Empyrean II with a Co source, a theta-theta goniometer, parallel beam optics, point focus in reflection mode, with a Xcelerator PASS detector operating from 45-120 2θ for a 105-minute scan using a XYZ stage.

Scanning electron microscopy (SEM) and energy dispersity X-ray spectroscopy (EDS): SEM images and EDS maps were taken on a FEI Nova NanoSEM 630 SEM with an accelerating voltage of 7 keV for imaging and 15 keV for EDS. Samples for SEM analysis were coated with a 5 nm layer of iridium metal to prevent charge build-up. EDS analysis has a sample penetration depth of 2 μm under the surface and an error of ±5%.

Transmission electron microscopy (TEM): Particles of the laser-deposited samples were scratched off the surface, dispersed in ethanol, and ultrasonicated for 30 s. The particle dispersion was then drop-cast onto the TEM grid. High resolution TEM (HRTEM) and scanning TEM/electron dispersive spectroscopy (STEM-EDS) of the sample was performed using a FEI Titan G2 60-300 microscope at Penn State, operated at 80 and 200 kV with double spherical aberration correction, offering sub-angstrom image resolution. A high angle annular dark field (HAADF) detector with a collection angle of 42-244 mrad, camera length of 115 mm, beam current of 45 pA, beam convergence of 30 mrad, were used for STEM image acquisition and EDS data collection.

X-ray photoelectron spectroscopy (XPS): Data was collected using Physical Electronics PHI VersaProbe II. Samples were pumped to pressures of ~10^{-10} Torr and irradiated using monochromatic Al *K a* X-ray source (15 kV, ~48W). The survey and high-resolution spectra were recorded with pass energies of 187 and 46 eV, with step sizes of 0.8 and 0.2 eV, respectively. Charge neutralizers were used during all acquisitions. All spectra were charge referenced with respect to adventitious carbon peak at 284.8 eV.[29,30]

For the depth profile, the sample was etched/sputtered using an Ar^+ ion beam with an energy of 2kV scanned over a 2 mm by 2 mm area. Sputter time intervals were 10 minutes and sputtering was carried out for a total of 120 minutes. These conditions correspond to an etch rate of 10nm/minute for SiO_2 on Si substrate. The exact etch rate of the samples analyzed are not known due to the absence of a reference and the roughness of the sample. However, it is assumed that the etch rate of the analyzed samples are lower than that of SiO_2 based on metal oxide samples studied. Depth profile spectra were recorded using pass energy of 117.4 eV with a step size of 0.5eV.

All XPS data were analyzed with CasaXPS Version 2.3.23.PR1.0.[44] All peaks except for nickel were all fitted using an Iterated Shirley background subtraction using an asymmetric Lorentzian lineshape LF(1,1,255,380,5).[29,30,44] Ni peaks were fitted using a default background subtraction using the same LF lineshape as the others. Peaks were fitted using binding energy and full width at half max (FWHM) values obtained from databases and relevant literature.[24–26,29,30,32,44] XPS data analysis has a penetration depth of 30 nm and a known error of 5-10%. Uncertainties in background subtraction and peak fittings were all calculated using a Monte Carlo approach in CasaXPS.[44,45]Electrochemical characterization: The as-deposited catalyst samples on FTO (6-8 Ω) were directly used as the working electrode. The electrolyte used for OER measurement was 1 M KOH with a Pt wire as the counter electrode and a saturated silver chloride electrode (SCE) as the reference electrode using a Versa STAT 4 potentiostat. The scan rate of linear sweep voltammetry (LSV) was 5 mV s^{-1} with iR-compensation, from 0 V to 1 V (*vs*. SCE). To stabilize the electrode surface, the electrode was cycled three times before data collection. Electric impedance spectroscopy (EIS) was performed in the same configuration at an overpotential of 30 mV, and the frequency range was 10 kHz. The electrochemical active surface area (ECSA) was determined by measuring the capacitive current associated with double-layer charging from the scan-rate dependence of cyclic voltammetry (CV) with the same working electrodes. ECSA is proportional to the slope of the capacitive current vs. scan rate. The potential window of CV was from -0.25 to -0.15 V (*vs.* SCE, 1M KOH), and the scan rates were 10, 20, 30, 40, 50, 60, 70, 80, 90, and 100 mV s^{-1}. The double layer capacitance (C_{dl}) was estimated by plotting the Δj at 0.2 V (*vs.* SCE) against the scan rate. The slope is twice of the C_{dl}.

In Situ Raman spectroelectrochemical measurements: The Raman spectroelectrochemical measurements were conducted using an *in Situ* Raman cell (Redox.me, Inc.) with 1 M KOH as the electrolyte, the catalyst synthesized *via* the LITV method deposited on FTO glass as the working electrode, an Ag/AgCl as the reference electrode, and Au wire as the counter electrode. The wavelength used for Raman measurements was 532 nm. Prior to the *in Situ* Raman spectroelectrochemical measurements, the electrodes were stabilized after 5 OER cycles.[40] Since the sample surface is cooled by the electrolyte, any laser annealing effects from the Raman analysis itself were observed to be significantly suppressed.

Turnover Frequency (TOF) Equations 1-3 for determining intrinsic OER electrocatalytic activity

TOF is calculated based on the assumption that all the 3d metal atoms (Fe, Co, and Ni) are considered as the active sites. Metal concentration was obtained by the XPS depth profile survey spectra shown in **Figure S3**. Total weight of the catalyst is 0.083 mg, and the area of the catalyst is 0.01 cm^{-2}.

$$\mathrm{TOF} = \frac{\text{Total oxygen turnovers per geometric area}}{\text{The number of metal active sites}} \quad (1)$$

$$\text{Number of Metal active sites} = \sum \frac{\text{Metal loading on the electrode (g cm}^{-2}\text{)} \times \text{Metal concentration (wt.\%)} \times 6.022 \times 10^{23}\ \text{mol}^{-1}}{\text{Metal atomic weight (g mol}^{-1}\text{)}} \quad (2)$$

Total oxygen turnovers

$$= |\text{j mA cm}^{-2}| \times \left(\frac{1\ \text{C s}^{-1}}{1000\ \text{mA}}\right) \times \left(\frac{1\ \text{mol e}^{-1}}{96485.3\ \text{C}}\right) \times \left(\frac{1\ \text{mol}}{4\ \text{mol e}^{-1}}\right) \times \left(\frac{6.022 \times 10^{23}\ \text{molecules O}_2}{1\ \text{mol O}_2}\right) \quad (3)$$

For example, the best performing sample **catalyst 1**, when the overpotential is 350 mV, j is 1450.2916 mA cm^{-2}.

Number of Total Metal active sites

$$= \text{Total metals (mol cm}^{-2}) \times (6.022 \times 10^{23}\ \text{mol}^{-1}) = 0.000145693 \times (6.022 \times 10^{23}\ \text{mol}^{-1}) = 8.77\text{E}19\ \text{cm}^{-2}$$

Total oxygen turnovers

$$= |1450.2916\ \text{mA cm}^{-2}| \times \left(\frac{1\ \text{C s}^{-1}}{1000\ \text{mA}}\right) \times \left(\frac{1\ \text{mol e}^{-1}}{96485.3\ \text{C}}\right) \times \left(\frac{1\ \text{mol}}{4\ \text{mol e}^{-1}}\right) \times \left(\frac{6.022 \times 10^{23}\ \text{molecules O}_2}{1\ \text{mol O}_2}\right) = 2.26\text{E}18\ \text{cm}^{-2}\text{s}^{-1}$$

$$\mathrm{TOF} = \frac{\text{Total oxygen turnovers per geometric area}}{\text{The number of metal active sites per geometric area}} = \frac{2.26\text{E}18\ \text{cm}^{-2}\text{s}^{-1}}{8.77\text{E}19\ \text{cm}^{-2}} = 0.0258\ \text{s}^{-1}$$

Equations 4 and 5. Monte Carlo simulations for mapping probability of Fe in the catalyst structure.

To understand the formation of the secondary amorphous Fe phase a Monte Carlo simulation was carried out based on a ReaxFF formulation of Ni, Fe, and O.[46] The initial structure was a nano-particle consisting entirely of cubic nickel oxide. The Monte-Carlo parameterization consisted of two possible moves: the first is a switching mechanism where two ions switch positions this was chosen 90% of the time the move was then accepted based on the energy of the original and new state, U_n and U_{n+1} respectively. After the switch an energy minimization was done to insure reaching a new state that is representative of a real structure. The acceptance criterion is given as,

$$\exp\left[-\frac{U_{n+1} - U_n}{kT}\right] \geq \text{rand}\left[0,1\right]. \quad (4)$$

In which *k* is Boltzmann's constant and *T* is the temperature in which the Monte-Carlo exploration was carried out, in this case it was taken to be 1000 Kelvin. The second possible move is switching one cation (either Fe or Ni) for the alternative, this occurred 10% percent of the time and was always accepted. This parameterization was chosen to quickly explore the compositional space accurately while finding the most likely structure as a function of composition. This was repeated for 2000 iterations.

Every intermediate state was recorded though the exploration was only started from accepted states. The analysis of the most likely cation sublattice configuration was then carried out by finding the occupational probability,

$$p_n = \frac{\exp\left[-\frac{U_n}{kT}\right]}{\sum_{i=0}^{N}\exp\left[-\frac{U_i}{kT}\right]} \quad (5)$$

In which N is the number of states. This analysis is particularly useful because it allows for an extrapolation of temperature into regimes above and below the simulation temperature. In **Figure S13** is a normalized plot of the iron occupational probability as a function of the radius from the center and temperature.

Density functional calculations and overpotential estimation

The overpotential is estimated as the maximum thermodynamic barrier between these states minus the standard redox potential for the overall reaction.

$$\eta = \max(\Delta G_{OH^*}, \Delta G_{O^*}, \Delta G_{OOH^*}, \Delta G_{bare})/e - \phi_{STD}$$

Where ϕ_{STD} is the standard redox potential for the OER reaction, 1.23 V *vs.* RHE. This approximation is applied based on the Bell-Evans-Polanyi principle. The reactions used to calculate the barriers are given in **Fig. S14a**. Surfaces with exposed metal octahedra were used to calculate these reaction energies. The (100), (1-12), (1-11), (112) and (001) surfaces were used for the NiO, β-CoOOH, β-NiOOH, hexagonal CoOOH, and γ-FeOOH phases, respectively.

The compositional dependence of the overpotential was tested in the hexagonal CoOOH (P63/mmc) oxyhydroxide which yielded lowest overpotentials for ternary mixtures of Co, Fe, and Ni. Near surface alloy configurations were sampled in a 2x2x4 surface cell in the (112) orientation and are pictured in **Figure S14b**. Transition metal configurations were chosen such that subsurface Fe is present for various combinations of Co and Ni.

We calculate the reaction energies in **Figure S14a**. using the computational hydrogen electrode reference. The reaction energies explicitly are:

$$\Delta G_{OH*} = \frac{1}{2}G_{H_2} + G_{OH*} - G_{bare} - G_{H_2O},$$

$$\Delta G_{O*} = \frac{1}{2}G_{H_2} + G_{O*} - G_{OH*},$$

$$\Delta G_{OOH*} = \frac{1}{2}G_{H_2} + G_{OOH*} - G_{O*} - G_{H_2O},$$

$$\Delta G_{bare} = \frac{1}{2}G_{H_2} + G_{O_2} + G_{bare} - G_{OOH*} - G_{H_2O}\,,$$

where G_{H_2} is the DFT energy of the H_2molecule, G_{H_2O} is the DFT energy of the water molecule, and G_{O_2} is the DFT energy of the oxygen molecule. Other energies, G_i, are the DFT energies of the respective labeled reference state on the metal oxide surface. The volcano plot in **Figure 5b** shows the overpotentials as predicted DFT with isosurfaces derived from linear scaling relationships. The predicted reaction energies and overpotentials are reported for the different phases and compositions in **Table S3**.

For all calculations, the energies for the steps in the conventional single-site OER mechanism were calculated with a vacuum separation of 14 Å between the slab surfaces and forces were converged to a maximum of 50 meV/Å per atom. Surface DFT calculations were performed using the Vienna Ab-initio Simulation Package.[43] A plane wave basis was used with a kinetic energy cutoff of 520 eV along with projector augmented wave potentials to represent ion cores.[47] Calculations were done at the level of spin-polarized *meta*-GGA + U using rotationally invariant U corrections.[13,14] The Hubbard U corrections are determined using the values and mixing schemes in Ong *et al*.[48] A Monkhorst-pack kpoint mesh was used to sample the Brillouin zone with a reciprocal space density of 180 / $Å^{-3}$ with a small amount of smearing, 0.05 eV, to smooth electronic occupations. It was found that zero point and vibrational energy corrections did not significantly affect the overpotential for test structures.

The electronic structure of the active site strongly influences OER reaction energetics. It is expected that the laser written samples produce catalytic sites with varied environments; the crystal field splitting of these sites is modulated by local chemical fluctuations and structural distortions, **Figure S15**. Both of these effects are quantified, to an extent, by the distortion parameter in **Figure 5c** of the main text. The crystal field splitting induced by a more distorted active site octahedron can lower the *filled* d-band energies and lead to more overlap, and therefore hybridizations, with the adsorbate oxygen p-orbital as schemed in **Figure S15**. We make some simple connections between the electronic structure of the active site and the distortion to support this.

We use projected density of states (PDOS) calculated from relaxed ionic coordinates to extract the band energies of the active site transition metal as well as the adsorbate oxygen for the O* intermediate, shown in **Figure S16a** for *h*-CoOOH. Though it is difficult to project onto the e_g and t_{2g} orbitals in this crystal structure, the filling of the spin-up channel (deep blue bar in **Figure S16a**) roughly represents the filling of the t_{2g} orbitals due to the expected 3+ and 2+ high-spin oxidation states for cobalt. The energies of these low energy d-bands decrease sharply with increased active site distortion, **Figure S16b**. This indicates that the crystal field splitting induced by the distortion is lowering the d-orbital energy. Because the filling of the anti-bonding orbitals is relatively the same for the various transition metal compositions in *h*-CoOOH , the decrease in d-orbital energy results in a rough decrease in O* adsorption energy, **Figure S16c**, towards the optimal range of 0.6 - 1.6 eV.

ACKNOWLEDGEMENTS

S. McGee, Y. Lei, L. Zarar, M. Terrones thank the Institutes of Energy and the Environment seed grant program at Penn State, S. McGee and L. Zarzar thank the Packard Foundation through support from the Packard Fellowship for Science and Engineering. J. Goff, S. Sinnot, I. Dabo, acknowledge financial support from the U.S. Department of Energy, Office of Science, Basic Energy Sciences, CPIMS Program, under Award No. DE-SC0018646. N.N. Nova acknowledges financial support from the National Science Foundation Materials Research Science and Engineering Center for Nanoscale Science at Penn State University under grant NSF-DMR 1420620.

SUPPORTING INFORMATION AVAILABLE

Additional details of the electrochemical data, Raman, XRD, TEM and EDS data collection; as well as additional details of the Monte Carlo and DFT structures and computations are included in the Supplemental Information. Tables summarizing the EDS and electrochemical performance data of the samples and comparisons to other OER catalysts in literature are also described within the Supplemental Information.

The authors declare no competing financial interest. The Supporting Information is available free of charge *via* the Internet at http://pubs.acs.org.

REFERENCES

(1) Looney, B. Statistical Review of World Energy Globally Consistent Data on World Energy Markets. In *bp Statistical Review of World Energy*. BP p.I.c: London, 2020.

(2) Doyle, R. L.; Lyons, M. E. G. The Oxygen Evolution Reaction: Mechanistic Concepts and Catalyst Design. In *Photoelectrochemical Solar Fuel Production: From Basic Principles to Advanced Devices*; Springer International Publishing, 2016: New York City, 41–104. https://doi.org/10.1007/978-3-319-29641-8_2.

(3) Kim, J. S.; Kim, B.; Kim, H.; Kang, K. Recent Progress on Multimetal Oxide Catalysts for the Oxygen Evolution Reaction. *Adv. Energy Mater.* **2018**, *8*, 1–26. https://doi.org/10.1002/aenm.201702774.

(4) Zhang, B.; Zheng, X.; Voznyy, O.; Comin, R.; Bajdich, M.; García-Melchor, M.; Han, L.; Xu, J.; Liu, M.; Zheng, L.; De Arquer, F.; Dinh, C.; Fan, F.; Yuan, M.; Yassitepe, E.; Chen, N.; Regier, T.; Liu, P.; Li, Y.; De Luna, P.; *et al*. Homogeneously Dispersed Multimetal Oxygen-Evolving Catalysts. *Science.* **2016**, *352*, 333–337. https://doi.org/10.1126/science.aaf1525.

(5) Tahir, M.; Pan, L.; Idrees, F.; Zhang, X.; Wang, L.; Zou, J. J.; Wang, Z. L. Electrocatalytic Oxygen Evolution Reaction for Energy Conversion and Storage: A Comprehensive Review. *Nano Energy*. **2017**, 136–157. https://doi.org/10.1016/j.nanoen.2017.05.022.

(6) Song, F.; Hu, X. Exfoliation of Layered Double Hydroxides for Enhanced Oxygen Evolution Catalysis. *Nat. Commun.* **2014**, *5*, 4477. https://doi.org/10.1038/ncomms5477.

(7) Bates, M. K.; Jia, Q.; Doan, H.; Liang, W.; Mukerjee, S. Charge-Transfer Effects in Ni-Fe and Ni-Fe-Co Mixed-Metal Oxides for the Alkaline Oxygen Evolution Reaction. *ACS Catal.* **2016**, *6*, 155–161. https://doi.org/10.1021/acscatal.5b01481.

(8) Shin, H.; Xiao, H.; Goddard, W. A. *In Silico* Discovery of New Dopants for Fe-Doped Ni Oxyhydroxide (Ni_1- XFe_xOOH) Catalysts for Oxygen Evolution Reaction. *J. Am. Chem. Soc.* **2018**, *140*, 6745–6748. https://doi.org/10.1021/jacs.8b02225.

(9) Liang, Y.; Wang, H.; Zhou, J.; Li, Y.; Wang, J.; Regier, T.; Dai, H. Covalent Hybrid of Spinel Manganese-Cobalt Oxide and

Graphene as Advanced Oxygen Reduction Electrocatalysts. *J. Am. Chem. Soc.* **2012**, *134*, 3517–3523. https://doi.org/10.1021/ja210924t.

(10) Stevens, M. B.; Enman, L. J.; Korkus, E. H.; Zaffran, J.; Trang, C. D. M.; Asbury, J.; Kast, M. G.; Toroker, M. C.; Boettcher, S. W. Ternary Ni-Co-Fe Oxyhydroxide Oxygen Evolution Catalysts: Intrinsic Activity Trends, Electrical Conductivity, and Electronic Band Structure. *Nano Res.* **2019**, *12*, 2288–2295. https://doi.org/10.1007/s12274-019-2391-y.

(11) Li, X.; Wang, H.; Cui, Z.; Li, Y.; Xin, S.; Zhou, J.; Long, Y.; Jin, C.; Goodenough, J. B. Exceptional Oxygen Evolution Reactivities on $CaCoO_3$ and $SrCoO_3$. *Sci. Adv.* **2019**, *5*, 6262. https://doi.org/10.1126/sciadv.aav6262.

(12) Suntivich, J.; May, K. J.; Gasteiger, H. A.; Goodenough, J. B.; Shao-Horn, Y. A Perovskite Oxide Optimized for Oxygen Evolution Catalysis from Molecular Orbital Principles. *Science.* **2011**, *334*, 1383–1385. https://doi.org/10.1126/science.1212858.

(13) Hammer, B.; Hansen, L. B.; Norskov, J. K. Improved Adsorption Energetics within Density-Functional Theory Using Revised Perdew-Burke-Ernzerhof Functionals. *Phys. Rev. B* **1999**, *59*, 7413–7421. https://doi.org/10.1103/PhysRevB.59.7413.

(14) Dudarev, S. L.; Botton, G. A.; Savrasov, S. Y.; Humphreys, C. J.; Sutton, A. P. Electron-Energy-Loss Spectra and the Structural Stability of Nickel Oxide: An LSDA+U Study. *Phys. Rev. B* **1998**, *57*, 1505–1509. https://doi.org/10.1103/PhysRevB.57.1505.

(15) Friebel, D.; Louie, M. W.; Bajdich, M.; Sanwald, K. E.; Cai, Y.; Wise, A. M.; Cheng, M. J.; Sokaras, D.; Weng, T. C.; Alonso-Mori, R.; et al. Identification of Highly Active Fe Sites in (Ni,Fe)OOH for Electrocatalytic Water Splitting. *J. Am. Chem. Soc.* **2015**, *137*, 1305–1313. https://doi.org/10.1021/ja511559d.

(16) Gong, M.; Li, Y.; Wang, H.; Liang, Y.; Z. Wu, J.; Zhou, J.; Wang, J.; Regier, T.; Wei, F.; Dai, H. An Advanced Ni–Fe Layered Double Hydroxide Electrocatalyst for Water Oxidation. *J. Am. Chem. Soc.* **2013**, *135*, 8452–8455. https://doi.org/10.1021/ja4027715.

(17) Smith, R. D. L.; Prévot, M. S.; Fagan, R. D.; Zhang, Z.; Sedach, P. A.; Siu, M. K. J.; Trudel, S.; Berlinguette, C. P. Photochemical Route for Accessing Amorphous Metal Oxide Materials for Water Oxidation Catalysis. *Science.* **2013**, *340*, 60–63. https://doi.org/10.1126/science.1233638.

(18) Zhang, S. L.; Guan, B. Y.; Lu, X. F.; Xi, S.; Du, Y.; Lou, X. W. (David). Metal Atom-Doped Co_3O_4 Hierarchical Nanoplates for Electrocatalytic Oxygen Evolution. *Adv. Mater.* **2020**, *32*, 2002235. https://doi.org/https://doi.org/10.1002/adma.202002235.

(19) Wu, Z. P.; Lu, X. F.; Zang, S. Q.; Lou, X. W. Non-Noble-Metal-Based Electrocatalysts toward the Oxygen Evolution Reaction. *Adv. Funct. Mater.* **2020**, *30*, 1910274. https://doi.org/10.1002/adfm.201910274.

(20) Smith, R. D. L.; Prévot, M. S.; Fagan, R. D.; Trudel, S.; Berlinguette, C. P. Water Oxidation Catalysis: Electrocatalytic Response to Metal Stoichiometry in Amorphous Metal Oxide Films Containing Iron, Cobalt, and Nickel. *J. Am. Chem. Soc.* **2013**, *135*, 11580–11586. https://doi.org/10.1021/ja403102j.

(21) Nikam, S. M.; Sharma, A.; Rahaman, M.; Teli, A. M.; Mujawar, S. H.; Zahn, D. R. T.; Patil, P. S.; Sahoo, S. C.; Salvan, G.; Patil, P. B. Pulsed Laser Deposited $CoFe_2O_4$ Thin Films as Supercapacitor Electrodes. *RSC Adv.* **2020**, *10*, 19353–19359. https://doi.org/10.1039/D0RA02564J.

(22) Zarzar, L. D.; Swartzentruber, B. S.; Donovan, B. F.; Hopkins, P. E.; Kaehr, B. Using Laser-Induced Thermal Voxels to Pattern Diverse Materials at the Solid-Liquid Interface. *ACS Appl. Mater. Interfaces* **2016**, *8*, 21134–21139. https://doi.org/10.1021/acsami.6b06625.

(23) Kindle, C.; Castonguay, A.; McGee, S.; Tomko, J. A.; Hopkins, P. E.; Zarzar, L. D. Direct Laser Writing from Aqueous Precursors for Nano to Microscale Topographical Control, Integration, and Synthesis of Nanocrystalline Mixed Metal Oxides. *ACS Appl. Nano Mater.* **2019**, *2*, 2581–2586. https://doi.org/10.1021/acsanm.9b00360.

(24) Bai, L.; Wen, X.; Guan, J. Amorphous FeCoNi Oxide for Oxygen Evolution Reaction. *Mater. Today Energy* **2019**, *12*, 311–317. https://doi.org/https://doi.org/10.1016/j.mtener.2019.02.004.

(25) Li, Z.; Cai, L.; Song, M.; Shen, Y.; Wang, X.; Li, J.; Wang, J.; Wang, P.; Tian, L. Ternary FeCoNi Alloy Nanoparticles Embedded in N-Doped Carbon Nanotubes for Efficient Oxygen Evolution Reaction Electrocatalysis. *Electrochim. Acta* **2020**, *339*. https://doi.org/10.1016/j.electacta.2020.135886.

(26) López, M. C.; Ortiz, G. F.; Lavela, P.; Alcántara, R.; Tirado, J. L. Improved Energy Storage Solution Based on Hybrid Oxide Materials. *ACS Sustain. Chem. Eng.* **2013**, *1*, 46–56. https://doi.org/10.1021/sc300096s.

(27) Wu, Z.; Wang, X.; Huang, J.; Gao, F. A Co-Doped Ni–Fe Mixed Oxide Mesoporous Nanosheet Array with Low Overpotential and High Stability towards Overall Water Splitting. *J. Mater. Chem. A* **2018**, *6*, 167–178. https://doi.org/10.1039/C7TA07956G.

(28) Du, X.; Yao, T.-L.; Wei, Q.; Zhang, H.; Huang, Y. Investigation of Fe−Ni Mixed-Oxide Catalysts for the Reduction of NO by CO: Physicochemical Properties and Catalytic Performance. *Chem. – An Asian J.* **2019**, *14*, 2966–2978. https://doi.org/https://doi.org/10.1002/asia.201900782.

(29) NIST X-ray Photoelectron Spectroscopy Database. https://doi.org/10.18434/T4T88K,.

(30) Briggs, D. *X-Ray Photoelectron Spectroscopy (XPS)*. Eden Prairie: Minnesota., 2005. https://doi.org/10.1002/0470014229.ch22.

(31) Biesinger, M. C.; Payne, B. P.; Grosvenor, A. P.; Lau, L. W. M.; Gerson, A. R.; Smart, R. S. C. Resolving Surface Chemical States in XPS Analysis of First Row Transition Metals, Oxides and Hydroxides: Cr, Mn, Fe, Co and Ni. *Appl. Surf. Sci.* **2011**, *257*, 2717–2730. https://doi.org/10.1016/j.apsusc.2010.10.051.

(32) Budi, S.; Kurniawan, B.; Mott, D. M.; Maenosono, S.; Umar, A. A.; Manaf, A. Comparative Trial of Saccharin-Added Electrolyte for Improving the Structure of an Electrodeposited Magnetic FeCoNi Thin Film. *Thin Solid Films* **2017**, *642*, 51–57. https://doi.org/10.1016/j.tsf.2017.09.017.

(33) Pikula, T.; Oleszak, D.; Pękała, M. Hyperfine Interactions and Some Magnetic Properties of Nanocrystalline $Co_{40}Fe_{50}Ni_{10}$ and $Co_{50}Fe_{45}Ni_5$ Alloys Prepared by Mechanical Synthesis and Subsequently Heat Treated. *Acta Phys. Pol. A* **2011**, *119*, 52–55. https://doi.org/10.12693/APhysPolA.119.52.

(34) Wu, H. Q.; Xu, D. M.; Wang, Q.; Wang, Q. Y.; Su, G. Q.; Wei, X. W. Composition-Controlled Synthesis, Structure and Magnetic Properties of Ternary $Fe_xCo_yNi_{100-x-y}$ Alloys Attached on Carbon Nanotubes. *J. Alloys Compd.* **2008**, *463*, 78–83. https://doi.org/10.1016/j.jallcom.2007.09.073.

(35) Slack, G. A. Crystallography and Domain Walls in Antiferromagnetic NiO Crystals. *J. Appl. Phys.* **1960**, *31*, 1571.

(36) Yu, X. Y.; Feng, Y.; Guan, B.; Lou, X. W. D.; Paik, U. Carbon Coated Porous Nickel Phosphides Nanoplates for Highly Efficient Oxygen Evolution Reaction. *Energy Environ. Sci.* **2016**, *9*, 1246–1250. https://doi.org/10.1039/c6ee00100a.

(37) Hull, A. W. A New Method of X-Ray Crystal Analysis. *Phys. Rev.* **1917**, *10*, 661.

(38) Okudera, H.; Kihara, K.; Matsumoto, T. Temperature Dependence of Structure Parameters in Natural Magnetite: Single Crystal X-Ray Studies from 126 to 773 K. *Acta Crystallogr. Sect. B* **1996**, *52*, 450–457. https://doi.org/10.1107/S0108768196000845.

(39) Narkiewicz, U.; Podsiadły, M.; Jędrzejewski, R.; Pełech, I. Catalytic Decomposition of Hydrocarbons on Cobalt, Nickel and Iron Catalysts to Obtain Carbon Nanomaterials. *Appl. Catal. A Gen.* **2010**, *384*, 27–35. https://doi.org/10.1016/j.apcata.2010.05.050.

(40) Louie, M. W.; Bell, A. T. An Investigation of Thin-Film Ni-Fe Oxide Catalysts for the Electrochemical Evolution of Oxygen. *J. Am. Chem. Soc.* **2013**, *135*, 12329–12337. https://doi.org/10.1021/ja405351s.

(41) Kostecki, R. Electrochemical and *In Situ* Raman Spectroscopic Characterization of Nickel Hydroxide Electrodes. *J. Electrochem. Soc.* **1997**, *144*, 485. https://doi.org/10.1149/1.1837437.

(42) Yeo, B. S.; Bell, A. T. *In Situ* Raman Study of Nickel Oxide and Gold-Supported Nickel Oxide Catalysts for the Electrochemical Evolution of Oxygen. *J. Phys. Chem. C* **2012**, *116*, 8394–8400. https://doi.org/10.1021/jp3007415.

(43) Hafner, J. *Ab-Initio* Simulations of Materials Using VASP: Density-Functional Theory and Beyond. *J. Comput. Chem.* **2008**, *29*, 2044–2078. https://doi.org/10.1002/jcc.

(44) Fairely, N. CasaXPS Manual 2.3. 15 Getting Started with CasaXPS. *Casa Softw. Ltd* **2009**, 1–177.

(45) Cumpson, P. J.; Seah, M. P. Random Uncertainties in AES and XPS: I: Uncertainties in Peak Energies, Intensities and Areas Derived from Peak Synthesis. *Surf. Interface Anal.* **1992**, *18*, 345–360. https://doi.org/https://doi.org/10.1002/sia.740180508.

(46) Shin, Y. K.; Kwak, H.; Zou, C.; Vasenkov, A. V; van Duin, A. C. T. Development and Validation of a ReaxFF Reactive Force Field for Fe/Al/Ni Alloys: Molecular Dynamics Study of Elastic Constants, Diffusion, and Segregation. *J. Phys. Chem. A* **2012**, *116*, 12163–12174. https://doi.org/10.1021/jp308507x.

(47) Blöchl, P. E. Projector Augmented-Wave Method. *Phys. Rev. B* **1994**, *50*, 17953–17979. https://doi.org/10.1103/PhysRevB.50.17953.

(48) Ong, S. P.; Richards, W. D.; Jain, A.; Hautier, G.; Kocher, M.; Cholia, S.; Gunter, D.; Chevrier, V. L.; Persson, K. A.; Ceder, G. Python Materials Genomics (Pymatgen): A Robust, Open-Source Python Library for Materials Analysis. *Comput. Mater. Sci.* **2013**, *68*, 314–319. https://doi.org/https://doi.org/10.1016/j.commatsci.2012.10.028.